Strong Substrate Binding Modulates the Acoustic Quality Factors in Gold Nanodisks

Niklas Gross[1], Mahyar Madadi[2], Behnaz Ostovar[3], Pratiksha D. Dongare[3], Lauren A. McCarthy[1], Wei-Yi Chiang[1], Wei-Shun Chang[4], Naomi J. Halas[1,3,6,7], Christy F. Landes[1,3,5], John E. Sader[8], Stephan Link[1,3]*

[1]Department of Chemistry, Rice University, Houston TX, 77005, United States
[2]Department of Materials Physics, Research School of Physics, ANU College of Science, Canberra, ACT 2600, Australia
[3]Department of Electrical and Computer Engineering, Rice University, Houston TX, 77005, United States
[4]Department of Chemistry and Biochemistry, University of Massachusetts Dartmouth, North Dartmouth, Massachusetts 02747, United States
[5]Department of Chemical & Biomolecular Engineering, Rice University, Houston TX, 77005, United States
[6]Department of Bioengineering, Rice University, Houston TX, 77005, United States
[7]Department of Physics and Astronomy, Rice University, Houston TX, 77005, United States
[8]Graduate Aerospace Laboratories, California Institute of Technology, Pasadena CA, 91125, United States

Keywords: Single-Particle Spectroscopy, Pump-Probe Spectroscopy, Acoustic Vibrations, Surface Plasmon, Electron Beam Lithography

TOC Graphic

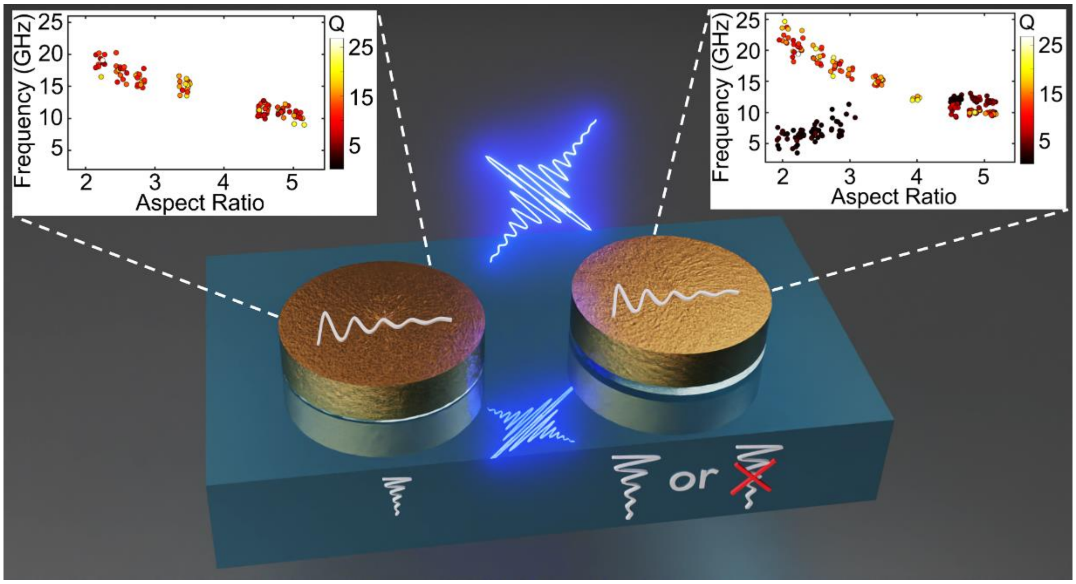

*To whom correspondence should be addressed: slink@rice.edu

Abstract

Lithographically prepared plasmonic nanoparticles are ideal mechanical probes, as their vibrational behavior can be precisely tuned through particle size and shape. But these particles exhibit strong intrinsic and extrinsic damping that results in small vibrational quality (Q) factors. Here, we perform single-particle transient transmission microscopy to investigate the effect of substrate-particle binding strength on the vibrational Q-Factor of lithographically prepared gold nanodisks on glass. Weak and strong binding is realized through titanium adhesion layers of variable thickness. We find that strong binding leads to the generation of several new acoustic modes with varying Q-Factors that depend on the particle aspect ratio and substrate material. Our work proposes an approach to tune enhanced acoustic Q-Factors of lithographically prepared nanoparticles and offers a comprehensive description of their damping mechanism.

Introduction

Nanostructures with coherent acoustic phonons in the GHz and THz regimes are ideal mechanical resonators.[1] Their acoustic frequencies and lifetimes depend sensitively on particle size, shape, and composition, as well as on the mechanical properties of the particle itself and its surroundings.[2-8] This sensitivity allows the design of resonators with specific acoustic characteristics and provides the ability to sense intrinsic and extrinsic changes to the resonator. Plasmonic nanoparticles are especially advantageous because they offer an all-optical way to access acoustic vibrations through their localized surface plasmon resonance (LSPR).[9-11] Based on these properties, nanoresonators have shown potential for applications in optomechanics,[12-15] biosensing,[16, 17] sensitive mass spectrometers,[18-22] and programmable devices.[23-25]

Short acoustic mode lifetimes limit the performance of nanoparticles in many applications. Intrinsic and extrinsic mechanical damping results in small vibrational Q-Factors.[11] Consistently larger Q-Factors were achieved for chemically grown plasmonic nanoparticles because intrinsic damping is reduced due to their higher degree of crystallinity. Specifically, Q-Factors of approximately 30 were found for substrate-supported single-crystalline aluminum nanoparticles.[26] Comparable Q-Factors between 20 and 30 were also observed for colloidal gold (Au) nanospheres and nanorods that were substrate-supported or optically trapped in water.[2, 27, 28] Further increased Q-Factor values were accomplished through distinct crystalline features or isolation from the environment. For example, Q-Factors up to 90 were found for aluminum crystals with a twin plane defect,[26] and single-crystalline Au nanoplates on unsupported thin films exhibited Q-Factors up to 75.[29] Five-fold twinned Au nanowires that were suspended over trenches showed Q-Factors reaching 100,[30, 31] and Q-factor up to 200 were achieved for Au nanoplates on lacey carbon films.[32]

Although lithographic techniques such as electron beam lithography produce polycrystalline nanostructures, they are nevertheless advantageous for the fabrication of mechanical nanoresonators, as they provide excellent control over particle dimension and shape, ensuring that all resonance frequencies are the same.[33-35] However, the ability to create nanoparticles with large Q-Factors through lithographic techniques is still disputed. Studies of lithographically prepared Au nanodisks (AuNDs) and nanorods found a constant Q-Factor of approximately 10,[28, 36] which was later also confirmed for aluminum nanodisks. Maximum Q-Factors around 10 were also reported for lithographically prepared Au nanorings on glass substrates.[26, 37] While these findings indicate that lithographically prepared metal nanoparticles do not offer large Q-Factors, other studies reported Q-Factor values between 20 and 30, reaching even as large as 50, for Au nanorods on glass substrates.[38] Similarly, AuNDs on sapphire substrates exhibited Q-Factors around 30 with some particles yielding maximum values up to 70.[39] Q-Factors approaching 70 were also accomplished for AuNDs on glass pillars.[40] These results indicate that lithographically prepared particles could indeed support increased Q-Factors and compete with colloidal nanostructures. Still, in order to reliably achieve large Q-Factors with lithographically prepared nanostructures and utilize them in applications, a comprehensive understanding of their damping behavior is required.

Single-particle transient transmission spectroscopy, coupled with finite element method (FEM) simulations, can resolve the acoustic properties of individual particles and determine the governing damping mechanisms.[3, 5, 6, 27, 31, 41-50] Using this approach, which eliminates artificial damping due to particle size variations, several studies of lithographically prepared AuNDs on a variety of substrates discussed whether the acoustic damping depends on the influence of the substrate or on particle crystallinity. On glass, acoustic behavior was previously reported to be strongly affected by intrinsic damping due to polycrystallinity,[51] leading to constant small Q-Factors independent of the substrate.[28] On the contrary, larger Q-Factors were achieved by placing AuNDs on glass pillars for reduced extrinsic damping into the substrate.[40] Despite experiencing intrinsic damping, AuNDs on sapphire substrates exhibited aspect ratio-dependent Q-Factor enhancements, which, under the assumption of strong particle-substrate binding, were theoretically attributed to reduced extrinsic damping due to mode hybridization effects.[39] Similar hybridization between acoustic modes of the particle and the substrate in the strong-binding regime was previously found for AuNDs on glass and Au nanocrosses on quartz substrates, but no Q-Factors were investigated.[34, 36]

These observations suggest that both intrinsic damping based on crystallinity and extrinsic damping based on substrate-induced losses must be considered in order to describe the acoustic behavior of plasmonic nanoresonators. More importantly, it appears that the substrate’s influence on extrinsic damping depends on its binding strength with the particle, raising the question of whether the desired Q-Factor enhancements could be intentionally generated through sample fabrication steps, such as the use of titanium (Ti) adhesion layers to control strong binding.[36] Although the ability to tune the Q-Factor of nanoparticles on different substrates through the binding strength presents an exciting possibility to overcome short acoustic mode lifetimes, this hypothesis has so far not been tested in detail.

Here, we applied single-particle transient transmission spectroscopy to investigate the Q-Factors of lithographically fabricated AuNDs on glass as a function of particle-substrate binding strength and aspect ratio. Ti adhesion layers of 2 nm and 4 nm were applied to achieve weak and strong binding between substrate and particle. In the case of strong binding, multiple acoustic modes with mode- and aspect ratio-dependent Q-Factors were observed. Using FEM simulations, we assign this behavior to the modification of acoustic modes through substrate-induced mechanical constraints in strongly bound particles. In contrast, we found a single acoustic mode with a lower and constant Q-Factor for weak binding. Based on these results, we propose a mechanism to tune acoustic Q-Factors in nanoparticles on glass and offer a comprehensive description of acoustic damping in substrate-supported lithographically prepared AuNDs.

Methods

Electron Beam Lithography

All AuNDs were fabricated using electron beam lithography. AuNDs with weak and strong binding on glass were fabricated with a thickness of 35 nm Au and Ti adhesion layers of 2 nm and 4 nm, respectively. 25x25x0.17 mm glass substrates (Corning, Product Number 2850-25) were used. The AuNDs had diameters between 70 nm and 178 nm. Each sample contained 16 particle arrays with rows of 15 particles per diameter. For sapphire substrates (25.4x25.4x0.2 mm, Advalue Technology, Item Code SS-C-S-RU2), no Ti layers were employed and the AuNDs had diameters between 91 nm and 178 nm.

For AuNDs with a 2 nm Ti layer, the substrate was cleaned by washing in an ultrasonic bath with a 2% (v/v) Hellmanex detergent, 190 proof ethanol, and ultrapure water for 10 minutes each. Subsequently, the substrates were dried under a stream of nitrogen and plasma etched with oxygen for 2 minutes. Then, the substrates were spin-coated with a layer of poly (methyl methacrylate) resist (PMMA 950 A2, MicroChem) and Espacer 300Z (Showa Denko) at 3000 revolutions per minute (rpm) each. Patterning of the resist was performed using the electron beam of a FEI QUANTA 650 SEM with a voltage of 30 kV and a beam current of 40 pA. The resist was developed in a methyl isobutyl ketone (MIBK): isopropyl alcohol (IPA) solution of ratio 1:3 (v/v). Using electron beam evaporation, metal layers were deposited on the substrate at a rate of 0.3 Å/s, with the thickness of the deposited layers monitored by a quartz crystal microbalance. The resulting structures were treated with a standard lift-off process by incubation in N-methyl-2-pyrrolidone at 65 °C for 2 hours. This fabrication was similar to our previous work.[28, 36] On sapphire, an almost identical procedure was performed. In this case, a thicker PMMA layer was spin-coated onto the substrate at 2500 rpm to accomplish better lift-off. While no Ti layer was deposited, the Au layer thickness was increased to 40 nm.

The same substrate cleaning process was applied for AuNDs with a 4 nm Ti layer. After plasma etching, the substrates were spin-coated at 4000 rpm for 1 minute with 950 poly (methyl methacrylate) A4 (Kayaku Advanced Materials), followed by a 2-minute bake on a 180-degrees Celsius hotplate. Afterward, the coverslips were spin-coated with the conductive polymer

Espacer 300Z (Showa Denko) at 3000 rpm for 1 minute and taken to an Elionix GLS-G100 electron beam writer operating at 100 kV and 1 nA. The patterns were developed by immersion for 65 seconds into a 1:3 (v/v) solution of MIBK:IPA, followed by a rinse in IPA. Metal layers were deposited at a rate of 0.3 Å/s using an electron beam evaporator. Finally, excess Au and Ti were removed by soaking the sample in acetone for 72 hours, followed by gentle sonication and drying under a nitrogen stream.

Single-Particle Transient Transmission Spectroscopy

Transient transmission spectroscopy was conducted on a homebuilt setup by combining an ultrafast pump-probe scheme with a single-particle microscope (Zeiss Axio Observer.D1m), as shown in Figure S1. The light source was a Ti:Sapphire oscillator (KMLabs Griffin-10) that was pumped by a 532 nm laser (Coherent Verdi G10), producing sub-100 fs light pulses at a frequency of 86 MHz and a center wavelength of 800 nm. The average output power of the oscillator was 1.05 W. A typical configuration includes 27% of the oscillator output being used for the pump beams, either at the fundamental frequency of the oscillator or at 400 nm after frequency doubling in a beta barium borate crystal (Altos BBO-1004H). For the probe beam, approximately 25% directed into a non-linear photonic crystal fiber (NKT Photonics FemtoWHITE 800) generate a white light continuum, with various bandpass filters available to select spectral slices of 25 nm as the probe within a wavelength range of 500-1000 nm. For all experiments discussed here, non-plasmon resonant excitation at 400 nm was used to excite Au interband transitions. Depending on the plasmon resonance position (Figure S2), the probe wavelength was varied between 600 and 800 nm to be close to the resonance, using either the spectrally filtered white light or 3% of the oscillator fundamental output directly as an alternative probe beam.

An optical delay stage (Newport UTS150CC) in the probe beam paths controlled the temporal overlap of the pump and probe pulses. The pump was modulated with an optical chopper (Newport 3502) at 10 kHz. Pump and probe beams were recombined using a dichroic mirror, focused onto the sample by an oil immersion (Zeiss Plan-Apochromat, 63x, 1.4 NA) or air (Zeiss EC-Epiplan Apochromat, 100x, 0.95 NA) objective with a high numerical aperture (NA) and collected by a receiving objective (Zeiss LD Achroplan, 40x, 0.6 NA) in a transmission geometry. The energy densities of the pump and probe beams at the sample were kept constant at approximately 4.75×10^4 and 1.59×10^4 W/cm^2 with beam sizes of 500 and 600 nm, respectively, in order to create the same initial electronic temperature change and hence prevent heat induced changes of the acoustic frequencies.[52] Optical filters were subsequently utilized to remove the pump beam, while the probe beam was detected by a photodiode (Femto DHPCA-100-F). The detected transmitted signal T was directed to a lock-in amplifier (EG&G Instruments Model 5302) that was referenced to the pump modulation frequency to read out changes in the pump-induced transmitted signal ΔT. ΔT was digitized with a data acquisition board (National Instruments USB-6229) and collected with a customized LabVIEW program. Using an oscilloscope (Tektronix TDS 2024C) to determine T from the photodiode, the differential transient transmission $\Delta T/T$ was obtained.

Transient transmission images were obtained by focusing the spatially and temporally overlapped pump and probe beams onto the sample, which was then scanned through the beams using a piezo scanning stage (Physik Instrumente P-517.3CL) (Figure S3). From the resulting image necessary for particle localization, single particles were placed in the beam path to measure $\Delta T/T$. To increase the signal-to-noise ratio, confirm the setup stability, and exclude possible perturbations such as thermal reshaping of the particle due to laser heating, time transients were repeated at least two times and averaged for each particle (Figure S4).

Hyperspectral Dark Field Scattering Spectroscopy

Single-particle scattering measurements were performed using an inverted microscope setup (Zeiss, Axio Observer m1). Light from a tungsten halogen lamp (Zeiss, Axioline HAL 100) was focused onto the sample using an oil-immersion condenser (Zeiss, Achromatic-aplanatic Condenser, Item Number 424208) in dark field mode. Scattered light from the AuNDs was collected with either a 50× magnification air-space objective lens (Zeiss EC Epiplan-NEOFLUAR, 50x, 0.8 NA) for smaller particles below 120 nm in diameter or a 74x reflective objective (Beck Optronic Solutions, Model 5007, 0.65 NA) for larger diameter AuNDs. The scattered light was directed into a spectrograph (Acton SpectraPro 2150i) and detected by a charge-coupled device (CCD) camera (Princeton Instruments PIXIS 400BR) after dispersion. A spectrograph and a CCD camera were mounted on a scanning stage that was driven by a linear actuator (Newport LTA-HL). Spectrally resolved images were measured by scanning the spectrograph over the field of view while collecting light through a slit aperture. The acquisition was controlled by a customized LabVIEW program. Dark-field scattering spectra were taken before and after transient transmission measurements to identify the plasmon resonance energies of the AuNDs and to ensure the absence of potential photothermal damage.

Finite Element Method Simulations

Finite element method simulations were performed to theoretically investigate the experimental results. Equation S1 in Note S1 was implemented in the commercial finite element modeling software COMSOL Multiphysics, using its eigenfrequency solver. Calculations were performed for AuNDs of various aspect ratios and with Ti thicknesses of 0 nm, 2 nm, and 4 nm.

Three computational scenarios of AuNDs were simulated to study the effect of the particle-substrate binding strength on the acoustic mode shape and frequency. First, the bottom surface of an AuND with a 2 nm Ti layer was modeled with free surface boundary conditions to simulate the case of minimum substrate influence. Second, the bottom surface of an AuND with a 4 nm Ti layer was modeled to be in rigid contact with the substrate to simulate the other case of strong substrate influence. The scenario of rigid binding was also repeated for an AuND directly on a sapphire substrate. Third, we studied the acoustic vibrations in long Au cylinders as a model system for AuNDs with small aspect ratios below 1.

For numerical simulations, the symmetry of AuNDs allowed the computational domain to be reduced to the r–z plane only (2D-axisymmetric modeling). The z-direction was directed along the thickness (height) of the disk, r was along the disk's radius, and the origin was in the center of the bottom surface of the Ti layer. To model elastic behavior of the much thicker glass layer and prevent reflections, perfectly matched layers on the bottom of the glass substrate were used to absorb propagating acoustic waves. We further assumed the substrate to be a half-sphere with a flat upper surface and a semi-infinite radius compared to the AuND. This geometry is illustrated in Figure S5.

The FEM simulations were performed for a frequency interval from 0 to 50 GHz, resulting in a multitude of acoustic modes of both the AuNDs and the environment. The simulated acoustic modes presented in Figures 3-6 were selected by mapping the Q-Factors in frequency-versus-aspect ratio plots, and identifying continuous traces of enhanced Q-Factors in the frequency range of the experimentally observed modes. This methodology is in line with previous literature.[53]

Results and Discussion

Transient transmission microscopy was used to resolve the acoustic vibrations of individual AuNDs on glass for different substrate-particle binding strengths. Figure 1a shows how we utilized Ti adhesion layers to control the binding strength of AuNDs to a glass support. Based on our previous work, Ti adhesion layer thicknesses of $t_{Ti} = 2$ nm and 4 nm were employed to establish weak and strong binding, respectively.[36] The AuND aspect ratio, defined as the ratio of disk diameter and thickness, was tuned by varying the diameter d_{Au} and maintaining a constant thickness $t_{Au} = 35$ nm. All particle morphologies were confirmed using scanning electron microscopy (SEM) images (Figure S6). A representative transient of an AuND with an aspect ratio of 3.4 and a Ti adhesion layer of 4 nm is displayed in Figure 1b. Each AuND exhibited an initial fast rise and decay as illustrated, representing electron-electron and electron-phonon scattering, respectively, to quickly heat the AuNDs.[11] This part of the signal was ignored, while we instead concentrated on the damped oscillations at longer pump-probe delay times. These oscillations reflected the damped acoustic vibrations that were launched impulsively by ultrafast laser heating of the AuND, and were accompanied by an overall exponential decay due to radiation of heat into the environment.[10]

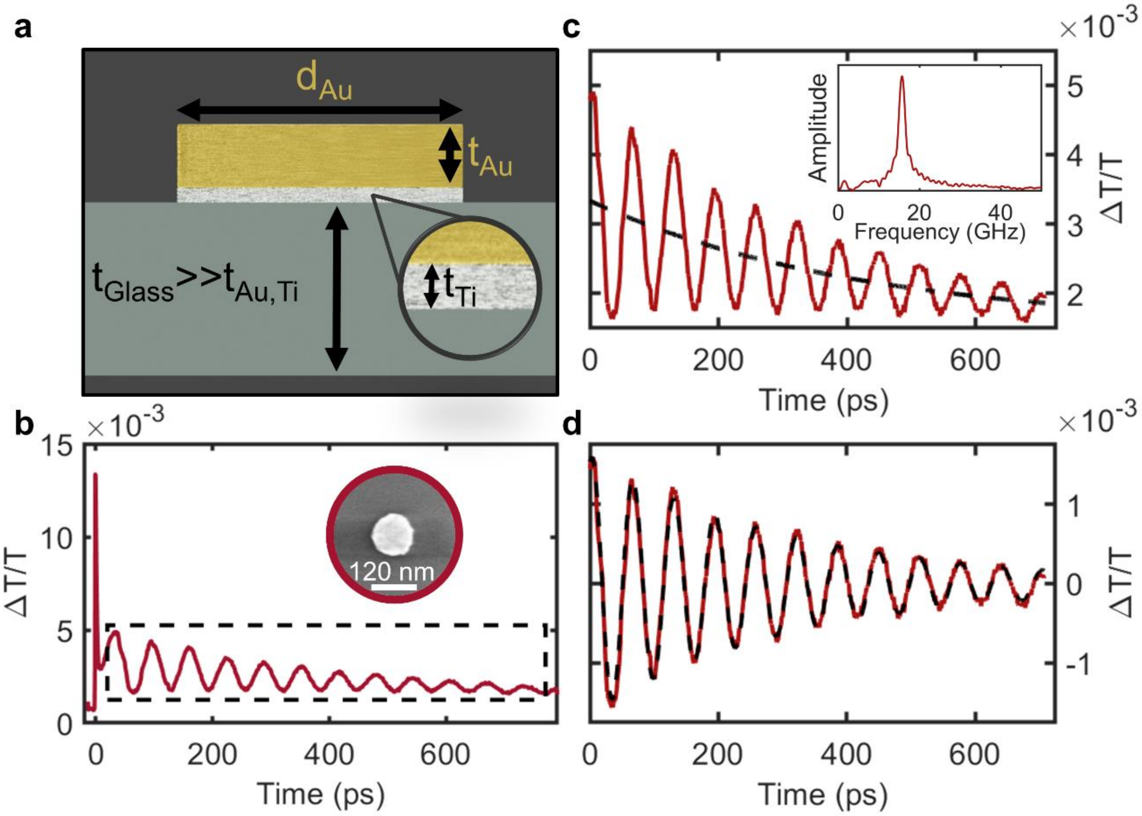

Figure 1: Transient transmission microscopy resolved the acoustic vibrations of single AuNDs. a) AuNDs were characterized by their aspect ratio, determined by a variable diameter d_{Au} and a constant thickness t_{Au}. A Ti adhesion layer of thickness t_{Ti} was applied between particle and substrate to vary the binding strength. The thickness of the underlying glass substrate t_{Glass} was considered semi-infinite compared to Au and Ti. b) Representative transient transmission of an AuND with an aspect ratio of 3.4 and a Ti adhesion layer of 4 nm. Radiation of heat into the environment caused a slow overall signal decay. The oscillating part of the transient (black box) contained information about the acoustic vibrations, and was subject to further analysis in c) and d). Inset: SEM image of the measured single AuND. C) An exponential function corresponding to the first term in equation 1 (black, dashed) was fit to the signal (red) and subsequently subtracted to eliminate the decay component due to heat loss. Inset:

Power spectrum obtained by the Fourier transform of the signal residuals after subtraction of the exponential fit to obtain the frequency components of the oscillation. D) The fit of a damped cosine function (black, dashed) to the residuals (red) from C) yielded the oscillation frequencies and damping times. The damped cosine functions are represented by the second term in equation 1.

We analyzed only the oscillatory part of the transient (Figure 1b, black box) to quantify acoustic vibration frequencies and damping times. An exponential fit was used to account for the decay component due to heat loss, as demonstrated in Figure 1c. After subtracting this exponential decay, a Fourier transform was applied to the residuals to yield the acoustic frequency components, as shown in the inset of Figure 1c. The extracted frequency components were improved upon by using them as starting values for a least-squares fit of an adjustable sum of damped cosine functions to the residuals, as presented in Figure 1d. Using the results of both fits, the exponential and damped cosine functions were combined and a final least-squares optimization was performed on the raw experimental data, according to:

$$\frac{\Delta T}{T}(t) = A \exp\left(-\frac{t}{\tau_a}\right) + \sum B \exp\left(-\frac{t}{\tau_b}\right) \cdot \cos(2\pi\nu t + \phi) + C, \tag{1}$$

where ΔT/T (t) is the differential transmission as a function of time delay t; ν is the acoustic frequency with a phase ϕ; τ_a and τ_b are the decay time for lattice cooling and the damping time of the acoustic vibrations, respectively; A and B are adjustable amplitudes; whereas C is a constant offset that accounts for the signal not completely decaying within the measurement window. The first term in equation 1 describes lattice cooling to the environment. The second term describes the acoustic vibrations and was expanded from a single to multiple damped cosine functions to account for varying numbers of acoustic modes. The extracted damping times τ_b and frequencies ν were used to calculate the vibrational quality factor $\mathrm{Q} = \pi\tau_\mathrm{b}\nu$. Using this methodology, we determined a Q-Factor of 15.2 ± 3.2 for the acoustic mode of AuNDs with an aspect ratio of 3.4 and a 4 nm Ti layer, as shown in Figure 1. This Q-Factor was slightly larger than the previously reported $Q \approx 11$ for similar AuNDs on Ti layers of 2 nm,[28] indicating a possible change in acoustic behavior due to the increased binding strength. All errors specified within this work correspond to the standard deviation from at least 5 measured particles for each aspect ratio.

The substrate-particle binding strength affects the acoustic frequencies and modes of AuNDs. Figure 2 shows representative differential transmission transients and corresponding power spectra of weakly and strongly bound AuNDs with aspect ratios of 2.2, 3.4, and 4.6. All weakly bound AuNDs exhibited a single acoustic mode as indicated by the absence of beating patterns in the transients (Figure 2a-c) and confirmed by a single peak in the power spectra given in the insets. With values of 18.8 ± 1.1 GHz, 15.1 ± 0.9 GHz, and 11.3 ± 0.7 GHz, the acoustic frequency of this mode decreased with increasing aspect ratio.

In contrast, strongly bound AuNDs had either one or two acoustic modes depending on the aspect ratio (Figure 2d-f). AuNDs with an aspect ratio of 2.2 exhibited a beating in the transients (Figure 2d), suggesting the existence of an additional mode. The corresponding power spectrum confirmed that two modes were present, with frequencies of 6.2 ± 0.9 GHz and 20.5 ± 1.3 GHz. The transients of strongly bound particles with an aspect ratio of 3.4 mainly displayed a similar behavior to their weakly bound counterparts with only one dominant frequency component of 15.1 ± 0.5 GHz, as already illustrated in Figure 1. However, a few AuNDs of this aspect ratio revealed a small side peak at smaller frequencies in the power spectrum, as shown in the inset of Figure 2e, indicating a second acoustic mode with almost similar frequency. The fact that only some AuNDs exhibited this behavior highlights the importance of a single-particle approach, as it is the only way to identify inter-particle variations. Larger, strongly bound AuNDs with an aspect ratio of 4.6 again showed distinct beating patterns in the transients, caused by two acoustic modes with comparable frequencies of 10.3 ± 0.8 GHz and 12.3 ± 0.4 GHz, also clearly visible in the power spectrum.

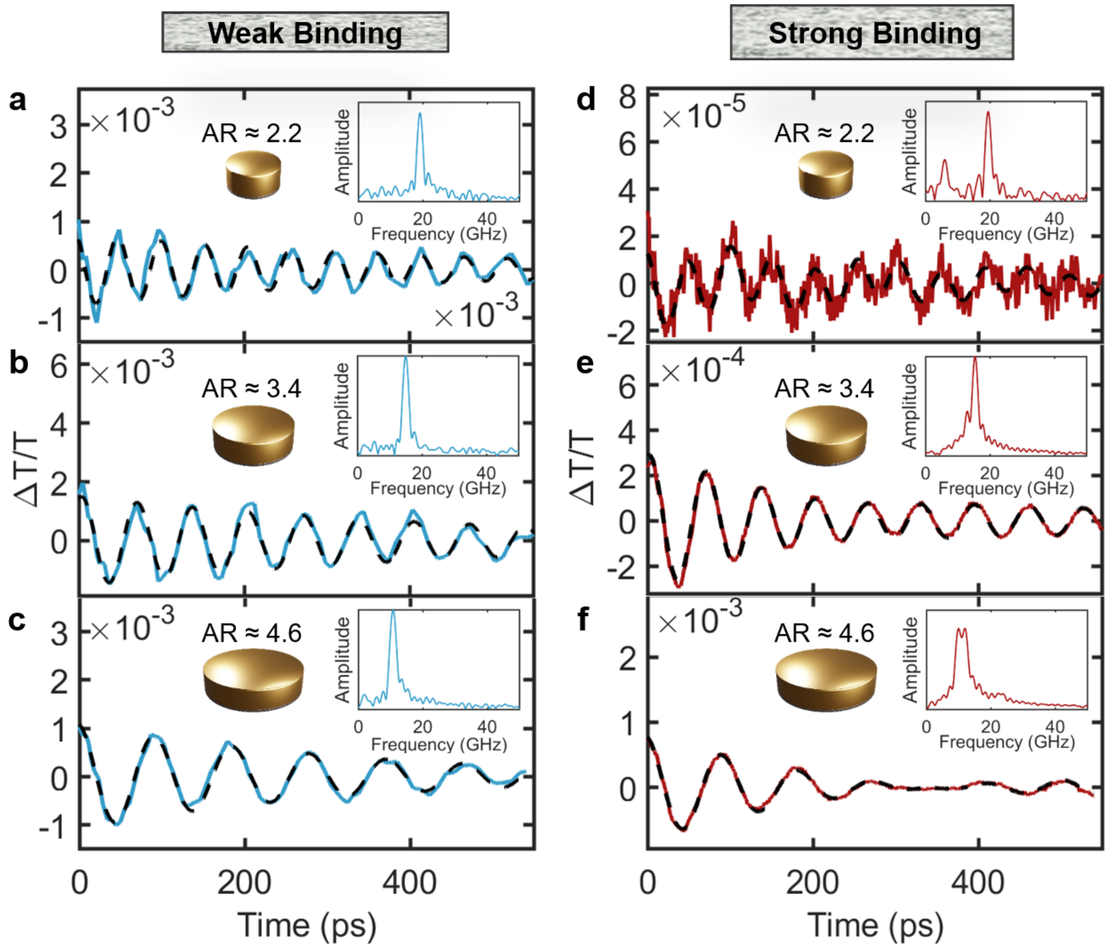

Figure 2: Strong coupling between AuNDs and a glass substrate induced an aspect ratio dependence of the acoustic modes. Weak binding (left): Oscillating component of the transient transmission for representative AuNDs with aspect ratios of 2.2 (a), 3.4 (b), and 4.6 (c) and a Ti adhesion layer of 2 nm. The black dashed lines represent the fit of a single damped cosine function to the data. Strong binding (right): Oscillating component of the transient transmission for representative AuNDs with aspect ratios of 2.2 (d), 3.4 (e), and 4.6 (f) and a Ti adhesion layer of 4 nm. Here, the black dashed lines represent the fit of a combination of two damped cosine functions to the data. Insets: Power spectra

of the oscillating components generated by Fourier transform of the experimental data. For better visibility, the aspect ratio was abbreviated as AR.

The data in Figure 2 suggest that strong binding was accomplished through the thicker Ti adhesion layer, altering the acoustic behavior of the AuNDs. For weak binding, the steady frequency decrease of the single observed acoustic mode with increasing aspect ratio is in good agreement with previous reports of in-plane breathing mode observations and theoretical simulations.[28, 36, 54] In the case of strong binding, the higher frequency mode also exhibited decreasing frequencies with increasing aspect ratios, comparable to the in-plane breathing mode for weakly bound AuNDs, whereas the low-frequency mode did not follow a clear trend. These findings are consistent with previous reports of strongly bound AuNDs that supported additional acoustic modes apart from the breathing mode.[36, 39]

The acoustic frequencies and Q-Factors of weakly and strongly bound AuNDs were determined for aspect ratios between 2 and 5 to better map out the effect the aspect ratio has on acoustic mode frequencies and damping. As a baseline, we first investigated the acoustic mode for the case of weak particle-substrate binding. Figure 3a illustrates the experimental acoustic frequencies of individual weakly bound AuNDs, plotted against their aspect ratio and color-coded with their respective Q-Factor. All 112 AuNDs measured supported only a single mode with a frequency that decreased from ~20 GHz for an aspect ratio of 2 to ~10 GHz for an aspect ratio of 5. The average Q-Factor was 13.2 ± 4.5 over the entire aspect ratio range. Frequencies and Q-Factors for individual aspect ratios are provided in the supporting information (Table S1).

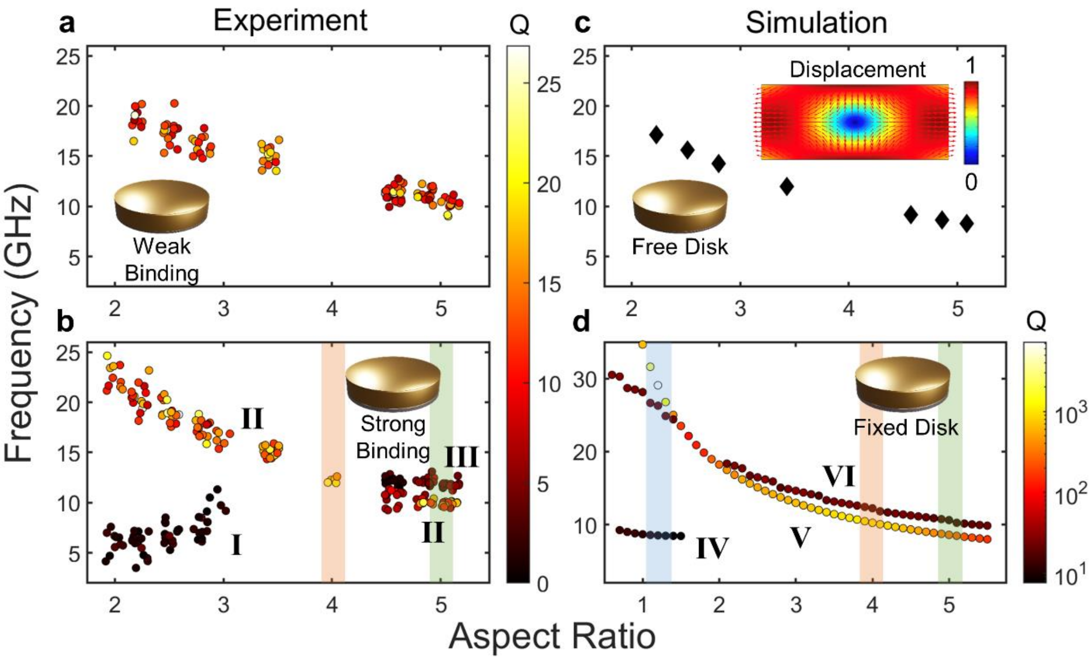

Figure 3: Strong particle-substrate binding led to enhanced Q-Factors at specific aspect ratios. a) Experimental acoustic frequencies of individual AuNDs on glass with a 2 nm Ti adhesion layer plotted against the AuND aspect ratio. The data points are color-coded with the value of the Q-Factor. b) Experimentally determined acoustic frequencies of individual AuNDs on glass with a 4 nm Ti adhesion layer plotted against the AuND aspect ratio. The data points are color-coded with the value of the Q-Factor. Orange and green bars mark areas of interest for comparison with simulated results. Modes **I**, **II**, and **III** were identified as discussed in the text. For better visualization in a) and b), a small x-offset was applied within each group of data points corresponding to the same aspect ratio. See tables S1 and S2 for specific aspect ratios and the corresponding average Q-Factors. c) FEM simulated acoustic frequencies of the in-plane breathing mode of unbound (free) AuNDs with varying aspect ratios. No substrate was considered, leading to zero damping and no determination of extrinsic Q-Factors. Inset: Displacement profile of the in-plane breathing mode. Blue to red colors indicate increasing displacement, while arrows indicate displacement direction. D) FEM simulated acoustic frequencies and Q-Factors of strongly bound (fixed) AuNDs with a 4 nm Ti layer as a function of aspect ratio. The bimetallic AuNDs were considered to be in perfect mechanical contact with the glass substrate. Blue, orange, and green bars mark areas of

interest for further analysis and comparison with experimental results. Modes **IV**, **V**, and **VI** were identified.

In contrast, strongly bound AuNDs supported three distinct acoustic modes with different Q-Factors depending on the aspect ratio. Figure 3b summarizes the experimental results. Two modes, labeled **I** and **II**, were observed for small aspect ratios up to ~3, with frequencies of about 5-10 GHz and 15-25 GHz, respectively. The average Q-Factors within this aspect ratio regime were 2.4 ± 1.9 for mode **I** and 15.0 ± 2.0 for mode **II**. For aspect ratios between 3 and 4.5, only mode **II** was seen with an average Q-Factor of 17.0 ± 2.6, which represents a maximum for mode **II**. For the largest aspect ratios from 4.5 to 5, mode **II** and an additional mode **III** were visible. While Mode **II** had a similar average Q-Factor of 12.2 ±.4.4 as seen for the smallest aspect ratios, the average value for mode **III** was determined to be only 4.3 ±.2.6. Both modes **II** and **III** had similar frequencies with an average frequency difference of only 2.0 ± 0.1 GHz. Frequencies and Q-Factors for individual aspect ratios are again provided in the supporting information (Table S2).

FEM simulations were performed and compared to the experimental data to assign the different acoustic modes and investigate their acoustic damping. The acoustic Q-Factor can be separated into intrinsic and extrinsic contributions, Q_{int} and Q_{ext}, according to:[11]

$$\frac{1}{Q} = \frac{1}{Q_{int}} + \frac{1}{Q_{ext}} \tag{2}$$

Intrinsic contributions describe the dissipation of vibrational energy due to, for example, particle crystallinity or density of grain boundaries and are generally larger for polycrystalline particles. Extrinsic contributions comprise losses of vibrational energy to the environment, such as the substrate, liquid media, and surface-bound ligands.[11] FEM simulations do not consider intrinsic damping mechanisms and the simulated Q-Factors correspond to Q_{ext}. Atomistic studies are required to consider defects, but are computationally expensive and have only been applied to much smaller systems.[55, 56] In the following discussion, we, therefore, refer to Q_{ext} when discussing simulated Q-Factors. Due to the exclusion of intrinsic damping, the simulated Q-Factors were generally much larger than the experimental values.

Considering that the in-plane breathing mode was experimentally observed for weakly bound AuNDs,[36] we calculated its acoustic frequencies for the limiting case of a free AuND. Figure 3c shows the simulated acoustic frequencies of the in-plane breathing mode of a free AuND, with values in the range of approximately 8-18 GHz. The experimental frequencies in Figure 3a were well described by these simulations. An average frequency difference of 2.1 ± 0.5 GHz over all aspect ratios was observed and attributed to the previously reported stiffening effect caused by the substrate, even in the case of weak binding.[36] Continuum mechanics describes a linear relationship between the acoustic frequency of the in-plane breathing mode of a free disk and its inverse diameter.[54, 57] Indeed, plotting the experimental frequencies against their inverse diameter yielded a linear relationship that agreed well with the simulations (Figure S7), further confirming our mode assignment. Since no extrinsic medium due to the surrounding air was considered in the FEM simulations, extrinsic Q-Factors due to hydrodynamic damping were not determined.

The good agreement between the experimental frequencies and the model of a free disk indicates a limited influence of the substrate in the case of weak binding. The inset of Figure 3c shows the calculated displacement profile of the in-plane breathing mode. Looking at the vertical AuND cross-section from the side, the profile illustrates the horizontal disk expansion during the in-plane breathing mode. The largely horizontal displacement suggests minimized transport of acoustic energy into the substrate, diminishing its influence in the experiment. Additionally, if efficient transport of acoustic energy between AuND and substrate had been established in the experiment, increased substrate damping should have occurred for larger aspect ratios due to their larger contact areas. The almost constant experimental Q-Factors for different aspect ratios (Figure S8) are thus consistent with weak coupling.

It is important that, while the experimental Q-Factors of weakly bound AuNDs did not exhibit clear trends with the aspect ratio, they showed particle-to-particle variations with Q-Factors ranging between 6 and 27. The average Q-Factor of 13.2 ± 4.5 measured here is good in agreement with our previous report of a constant value of 11.3 ± 2.5.[28] However, the increased standard deviation in the Q-Factor, amounting to 34% of the average value, indicates broader fluctuations. Assuming a minor influence of the substrate, we attribute the large Q-Factor variations to differences in intrinsic damping due to the heterogeneous polycrystalline nature of lithographically prepared structures. We hypothesize that the larger average Q-Factor and increased standard deviation observed are due to a few well-fabricated AuNDs with fewer internal defects, which support maximum Q-Factor values of ~27.

Simulations of strongly bound AuNDs on a glass substrate reproduced the experimental results. As illustrated in Figure 3d, three acoustic modes labeled **IV**, **V**, and **VI** were identified. Modes **V** and **VI** were present throughout the entire investigated aspect ratio range and crossed at an aspect ratio of ~1.6. Both modes had comparable frequencies, only deviating from each other by about 2 GHz on average and decreasing from 34 to 8 GHz as the aspect ratio increased from roughly 1 to 5.5. In contrast, mode **IV** was only observed up to an aspect ratio of approximately 1.5 with a constant frequency of 8.7 ± 0.3 GHz. The simulated Q-Factors varied strongly between modes and aspect ratios, with an overall minimum of ~10 and a maximum of

~7250. The lowest simulated Q-Factors were found for mode **IV**, which had an average value of 10.7 ± 2.5. Mode **VI** exhibited almost constant values of 23.4 ± 4.4 for all aspect ratios. Most importantly, mode **V** displayed generally larger Q-Factors than modes **IV** and **VI** and exhibited large Q-Factor enhancements with maximum values of ~7250 and ~1000 for aspect ratios of ~1.2 and ~4.

Before directly comparing the experimental and simulated data of strongly bound AuNDs, it is important to consider fundamental differences between the experimental and theoretical approaches. The largest simulated Q-Factors were two orders of magnitude larger than those seen in the experiment because intrinsic damping could not be considered, as mentioned above. In addition, a perfect mechanical contact between the particle and substrate was assumed in the simulation. While strong substrate binding for an adhesion layer thickness of 4 nm has previously been suggested,[36] crystal defects at the glass/Ti and Au/Ti interfaces due to the polycrystallinity of evaporated metal films could contribute to a deviation from perfect mechanical contact in the experiment. Then, the ability to accurately identify multiple acoustic modes in an experimental transient depends on their respective excitation and detection efficiencies as well as their lifetimes.[9, 39] Additional criteria are uncertainties in the fit analysis and the signal-to-noise ratio.[58] We, therefore, expect discrepancies between experiment and simulation for 1) smaller particles with smaller transient signals, 2) modes of similar frequency, and 3) short-lived or inefficiently excited and/or probed modes.

Mode **I** resembled mode **IV** in both frequencies and Q-Factors, indicating that a short-lived acoustic mode was excited for small aspect ratio AuNDs. It is important to point out, though, that modes **I** and **IV** were observed at different aspect ratios, shifted by a value of ~1. Additionally, a small frequency shift of about 3 GHz was observed. We partially attribute these differences to the short acoustic lifetime and the small particle sizes giving smaller signals, which made the experimental measurement of mode **I** challenging. However, the average frequency standard deviation over all aspect ratios of mode **I** was only 1.2 ± 0.5 GHz and thus smaller than 3 GHz. Therefore, we suggest that the frequency differences between modes **I** and **IV** were predominantly caused by an imperfect contact in the experiment, as described earlier.

Similarly, mode **II** showed clear similarities with mode **V**. Both modes, having comparable frequencies, exhibited a frequency decrease with increasing aspect ratio. Interestingly, the large Q-Factor enhancement of mode **V** at an aspect ratio of 4 was represented in the experiment. Mode **II** showed the largest experimentally observed Q-Factor for strongly bound AuNDs with 18.8 ± 2.3 at an aspect ratio of 4. An average frequency difference of 2.8 ± 1.3 GHz between modes **II** and **V** was found, potentially due to the non-ideal contact in the experiment. However, since the frequency difference increased from approximately 1.4 GHz to 4.3 GHz when going towards smaller aspect ratio AuNDs with weaker signals, we attribute it mainly to experimental uncertainties.

Mode **III** matched mode **VI** well but was experimentally challenging to resolve. The fact that mode **III** was only observed for the largest aspect ratio AuNDs was likely due to its similar frequencies compared to mode **II**. The interference of almost identical acoustic frequencies caused slow modulation patterns that required high signal-to-noise ratios and measurements with long pump-probe delay times. Thus, mode **III** could not be resolved for smaller aspect ratio AuNDs, for which the frequency difference between modes **II** and **III** became even smaller. Additionally, when fitting the experimental data to identify Q-Factors of modes **II** and **III,** the similar frequencies made an assignment of Q-Factors difficult despite their discrepancy of ~8, while having no effect on achieving an excellent fit quality. Since this discrepancy was also observed in the simulated Q-Factors of modes **V** and **VI,** with **V** having consistently the larger Q-Factor, the simulation guided the assignment of the experimentally determined Q-Factors to modes **II** and **III**.

The experimental and simulated acoustic frequencies and Q-Factors of strongly bound AuNDs showed good agreement, reaffirming that the additional acoustic modes and their modified Q-Factors are the result of substrate interactions in the strong binding regime. Because the simulations only considered extrinsic damping by the substrate and no intrinsic properties were tuned in the experiment, the different Q-Factors for specific modes and aspect ratios must be due to changes in the extrinsic damping. Our results are consistent with previous studies,[36, 39] but demonstrate for the first time the important role that substrate binding, here accomplished through the Ti adhesion layer, plays for lithographically prepared plasmonic nanostructures on glass. The Ti layer controls strong substrate binding and hence enables mode hybridization, as discussed more below, so that certain geometries, i.e., aspect ratios here, can be optimized to yield enhancements in Q-Factors by controlling extrinsic damping.

Even though extrinsic damping due to the substrate is the damping mechanism of interest in the strong binding regime, the overall smaller experimental Q-Factors relative to simulation suggest that intrinsic damping affected the measured acoustic lifetimes as well. Considering mode **II**, its average Q-Factors at each aspect ratio had standard deviations similar to the weakly bound AuNDs (Figures S8 and S9), indicating particle-to-particle variations in intrinsic damping due to heterogeneous polycrystallinity for strongly bound AuNDs as well. Additionally, the minimum and maximum Q-Factors for mode **II** were ~4 and ~28, respectively, while the Q-Factor average over the entire aspect ratio range amounted to 13.9. Therefore, apart from the moderate enhancement at an aspect ratio of about 4, the overall Q-Factors of strongly bound

AuNDs were comparable to those of the in-plane breathing mode for weakly bound AuNDs. In agreement with the literature, these findings indicate that intrinsic damping is always an important channel for acoustic energy loss in lithographically prepared AuND.[28, 39] Indeed, our results suggest that intrinsic damping can almost fully prevent strongly enhanced Q-Factors, despite reduced extrinsic damping, and needs to be accounted for in order to achieve the largest Q-Factors. Based on these results, it is most likely that the large variation in reported Q-Factors for lithographically prepared nanostructures,[28, 38, 39] ranging from ~10 to ~70, is caused by intricate details of their respective fabrication process that determines both substrate binding and, importantly, internal crystallinity.

Despite intrinsic damping playing a major role in our experiments, we used the simulations to understand how reduced extrinsic damping and thus Q enhancement is achieved for hybridized modes. Specifically, we studied the shapes of the modes **IV**, **V**, and **VI** and how they differ from the in-plane breathing mode of the unbound AuNDs. Simulated displacement profiles describe the direction and maximum amplitude of mechanical displacement that an acoustic mode causes in a particle and its substrate and provide detailed insight into the dependence of the Q-Factor on the acoustic mode and the aspect ratio. Figure 4 displays the displacement profiles of modes **IV**, **V**, and **VI** at aspect ratios 1.2 (light blue), 4 (orange), and 5 (green), using the same color-coding as in Figure 3d. These aspect ratios were chosen to consider cases of strongly enhanced as well as small Q-Factors and partially coincide with experimentally studied aspect ratios. In Figure 4, the displacement amplitude increases from blue to red, with arrows indicating the displacement direction. Black horizontal lines mark the interface between AuND and adhesion layer (top) and adhesion layer and substrate (bottom). In the following discussion of the displacement profiles we consider the Ti adhesion layer to be part of the AuND,[36] and term the interface between adhesion layer and substrate the AuND-substrate interface.

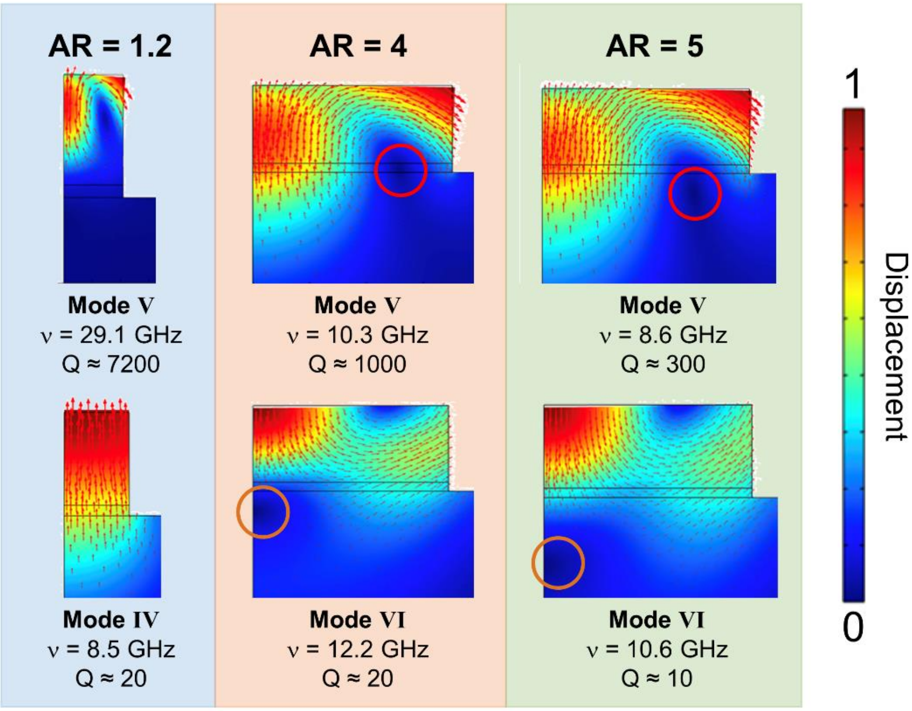

Figure 4: Enhanced Q-Factors were observed when displacement minima were located at the particle-substrate interface. Simulated displacement profiles of the acoustic modes **IV**, **V**, and **VI** labeled in Figure 3 at aspect ratios 1.2, 4, and 5. The normalized displacement is color-coded and increases from blue to red. Arrows indicate the displacement direction. The AuND symmetry was utilized to reduce computational cost. Thus, unlike the displacement profile in Figure 3, each side-view profile resembles the vertical cross-section of the right half of the AuND-substrate system, with the left edge corresponding to the AuND center. See Figure S5 for further visualization of the simulated geometry. For better visibility, the aspect ratio was abbreviated as AR.

The simulated displacement profiles deviated strongly from the in-plane breathing mode and were dependent on the aspect ratio. At an aspect ratio of 1.2, mode **V** resembled an edge mode in which the maximum displacement was concentrated in the top center and the edge of the disk

(Figure 4: light blue, top). Interestingly, the entire displacement seemed to be oriented in a circle, implying effective localization of acoustic energy inside the AuND. The corresponding Q-Factor was large, with a maximum value of ~7250. While the overall shape of the edge mode was maintained for aspect ratios 4 and 5 (Figure 4: orange and green, top), the displacement became more widespread and extended over both disk and substrate. For these aspect ratios, maximum displacement amplitudes were observed at the lower center and the upper edge of the AuND. Additionally, a distinct displacement minimum was located at the particle-substrate interface for aspect ratio 4, shifting slightly below the interface for aspect ratio 5 (red circles). The Q-Factor at aspect ratio 4 was smaller with a value of ~1000, but nevertheless presented a local maximum in the dependence of the Q-Factor on the aspect ratio for mode **V**. The Q-Factors further decreased for aspect ratios larger than 4, leading to a value of only ~300 at aspect ratio 5.

The shapes of mode **V** indicate that the acoustic Q-Factor is inversely related to the amount of displacement at the particle-substrate interface. Among the considered aspect ratios in Figure 4, the largest decrease in the Q-Factor of ~6200 for mode **V** occurred when the aspect ratio increased from 1.2 to 4. This observation can be attributed to the shift of the maximum displacement amplitude from the top of the AuND, where acoustic energy was conserved, towards the bottom of the AuND, where efficient transfer of acoustic energy into the substrate was enabled. However, there was no apparent change in the displacement amplitudes between aspect ratios 4 and 5, while the Q-Factor decreased by a value of ~700. Interestingly, the displacement minimum shifted from the AuND-substrate interface into the substrate, as indicated by the red circles in Figure 4, implying that even a spatially localized minimum in the displacement has an impact on the acoustic Q-Factor if located directly at the AuND-substrate interface. Thus, the reduced displacement directly at the AuND-substrate as compared to inside the AuND or the substrate appears to be most important, since it prevents or minimizes the transfer of acoustic energy out of the AuND and thus reduces extrinsic damping. This interpretation is further strengthened by the fact that the by far largest Q-Factor of ~7250 was found for mode **V** at an aspect ratio of 1.2, which showed the smallest displacements at the AuND-substrate interface for all discussed modes and aspect ratios.

The displacement profiles and associated Q-Factors for modes **IV** and **VI** are consistent with the above-proposed interface-mediated damping mechanism. At an aspect ratio of 1.2, mode **IV** exhibited a large displacement amplitude at the AuND-substrate interface, extending throughout the disk and into the substrate (Figure 4: light blue, bottom). The corresponding Q-Factor was only 20, as expected for acoustic energy being efficiently transferred into the substrate. The displacement profiles of mode **VI** were an inversion of mode **V** at aspect ratios 4 and 5 (Figure 4: orange and green, top and bottom), but showed smaller displacement maxima directly at the AuND-substrate interface than mode **V**. However, the corresponding Q-Factors of mode **VI** were only 20 and 10 at aspect ratio 4 and 5, respectively, smaller than for mode **V**. Following the above discussion, we attribute these reduced Q-Factors to a greater overall displacement at the AuND-substrate interface, since local minima were located further from the interface and closer to the particle center (orange circles).

The investigation of the acoustic mode profiles allowed us to identify the origin of substrate-induced Q-Factor enhancements in strongly bound AuNDs as the reduction of mechanical displacement at the AuND-substrate interface. First, strong binding creates hybridized acoustic modes for substrate-supported AuNDs with aspect ratio-dependent mode shapes. Enhanced Q-Factors then occur for aspect ratios at which these hybridized acoustic modes experience greatly reduced displacement at the AuND-substrate interface. For AuNDs on glass, two of such Q-

Factor enhancements were identified for mode **V** at aspect ratios of ~1.2 and ~4. Finally, we point out that similar Q-Factors were found for modes **IV** and **VI** at aspect ratios of 1.2 and 4, respectively, despite the much larger displacement at the AuND-substrate interface for mode **IV**. With the AuND-substrate interface area being much larger for bigger aspect ratios, this finding suggests that the total contact area between the AuND and the substrate also affects the transfer of acoustic energy and the magnitude of extrinsic damping, in contrast to our previous result for weak binding.[28]

To test the validity of our simulations as well as our hypothesis of interface-mediated extrinsic damping for strongly bound AuNDs, we performed simulations of rigidly bound AuNDs that were directly placed on a sapphire substrate. Such studies were reported previously and were chosen as a benchmark.[39] Figure 5a shows the simulated acoustic frequencies plotted against the aspect ratio and color-coded with the corresponding Q-Factor. Again, three acoustic modes, labeled **VII**, **VIII**, and **IX**, were observed. The overall trends were comparable to those on a glass substrate with frequency differences on the order of ~5 GHz. Mode **IX** was not observed for aspect ratios smaller than 2.6, where it intersected with mode **VIII**. Most importantly, Q-Factors of mode **VIII** ranged from ~50 to ~100 for aspect ratios above 3, but were enhanced for smaller aspect ratios with two maxima at aspect ratios of ~1.1 and ~2.1, where the Q-Factor increased to ~25000 and ~3000, respectively. In contrast, the Q-Factor of mode **VII** was small with maximum values of ~10, while mode **IX** exhibited a constant Q-Factor value of ~60. The calculated acoustic frequencies and, in particular, the second maximum in Q-Factors at an aspect ratio of ~2.1 agreed well with the literature,[39] validating our computational approach. However, both modes **VIII** and **IX** were reported to be present for the smallest aspect ratio AuNDs with similar frequencies but Q-Factors that differed by two orders of magnitude.

The near degeneracy of the acoustic frequencies likely concealed the existence of mode **IX** at aspect ratios below 3 here at the resolution of our simulations.

The displacement profiles of AuNDs on sapphire were comparable to those on glass. Figure 5b illustrates the displacement profiles of the simulated acoustic modes **VII** and **VIII** on sapphire for the aspect ratio of 2.1. This aspect ratio was chosen since it exhibited a maximum in Q-Factor and corresponds to the maximum for glass at AuND aspect ratio of 4, as explained further below. Modes **VII** and **VIII** resembled an out-of-plane mode and an edge mode that agreed well with the literature,[39] again confirming our simulations. These profiles clearly demonstrate how large and small displacements at the AuND-substrate interface lead to small and large Q-Factors for modes **VII** and **VIII**, respectively. The correlation between mode profiles and Q-Factor enhancement on both sapphire and glass supports our explanation of interface-mediated extrinsic damping, independent of substrate material, as long as strong binding is present.

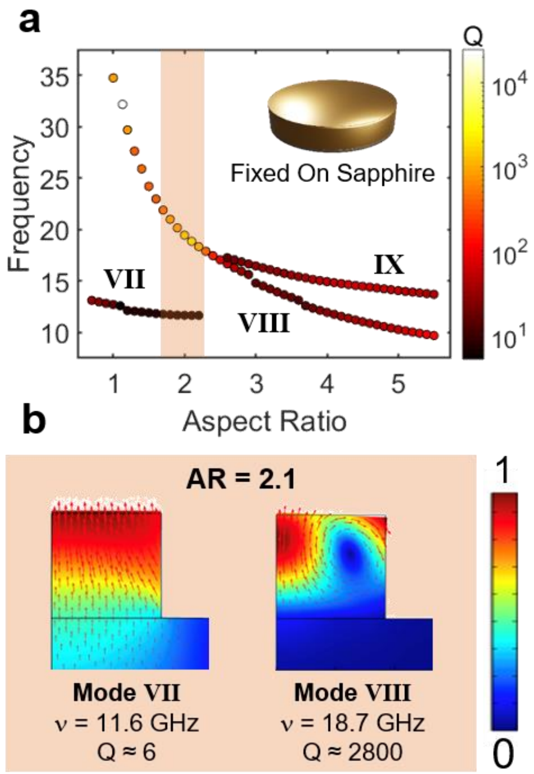

Figure 5: Strong binding of AuNDs on sapphire causes comparable Q-Factor enhancements. a) Simulated acoustic frequencies and Q-Factors of fixed AuNDs on a sapphire substrate plotted against the aspect ratio. Three modes labeled **VII**, **VIII**, and **IX** were observed. The disk was considered to be in perfect mechanical contact with the substrate. The orange bar marks an area of interest for further mode analysis in b). b) Displacement profiles of the acoustic modes **VII** and **VIII** for an aspect ratio of 2.1. The profiles are shown as vertical cross-sections of the right half of the AuND-substrate system. For better visibility, the aspect ratio was partially abbreviated as AR.

The comparison of AuNDs on sapphire and glass demonstrates that, under the assumption of strong binding, the acoustic modes and Q-Factors of AuNDs could be further tuned through the substrate material. The Q-Factor maxima of mode **V** on glass occurred at aspect ratios of ~1.2 and ~4, whereas those of mode **VIII** on sapphire were found at aspect ratios of ~1.1 and ~2.1. At the same time, the magnitudes of the Q-Factor maxima differed between AuNDs on sapphire and glass. Maximum Q-Factors of ~7250 and ~1000 were observed for the first and second maximum for AuNDs on glass, respectively, while Q-Factors of ~25000 and of ~3000 were obtained for AuNDs on sapphire. It is important to note that the Ti adhesion layer was omitted for the simulations of mode **VIII** on sapphire to validate our results against previous work.[39] However, the change from a bi-layered to a monometallic disk has been reported to cause only a frequency shift.[36] Therefore, the different Q-Factor maxima in terms of their aspect ratio and magnitude when switching from glass to sapphire must be due to the substrate material.

This comparison illustrates the importance of also considering the stress at the interface. Indeed, the Q-Factors of the discussed edge modes **V** (on glass) and **VIII** (on sapphire) were found to have a strong dependence on the relative acoustic impedances of the AuND and the substrate. Figure S10 illustrates how the smaller acoustic impedance mismatch between the AuND and the substrate leads to larger and narrower maxima at smaller aspect ratios. Here, the smaller acoustic impedance mismatch for the sapphire substrate resulted in larger Q-Factor maxima at smaller aspect ratios compared to glass. Therefore, for mode hybridization in the strong coupling regime, the choice of substrate and particle material offers the ability to engineer Q-Factor maxima at desired aspect ratios through control of their relative acoustic impedances.

The dependence of the Q-Factor on the displacement at the AuND-substrate interface can be understood with a simplified model of a long cylinder. Figure 6a shows the schematic of a long Au cylinder with a diameter of 40 nm and a height of 1000 nm on a sapphire substrate. Assuming an oscillating edge mode, illustrated in Figure 6b for an AuND with an aspect ratio of 2.1 on sapphire, mechanical displacement in the cylinder was calculated. Figure 6c displays the vertically directed displacement u_z caused by the edge mode at the center of the cylinder (r=0) and at different positions along the cylinder height in black. Using the cylinder diameter, the different height positions were translated into aspect ratios. The cylinder can therefore be regarded as a representation of many AuNDs with continuously increasing thicknesses. When moving along the cylinder height, effectively increasing the aspect ratio, an oscillatory behavior of u_z around zero displacement was observed, indicating a series of displacement nodes within the cylinder. For comparison, we also plotted the Q-Factors of the edge mode in AuNDs of the same aspect ratios on a sapphire substrate in red. Interestingly, the displacement nodes (i.e., zero displacement) in the cylinder aligned perfectly with the maxima in the calculated Q-Factors of the AuNDs.

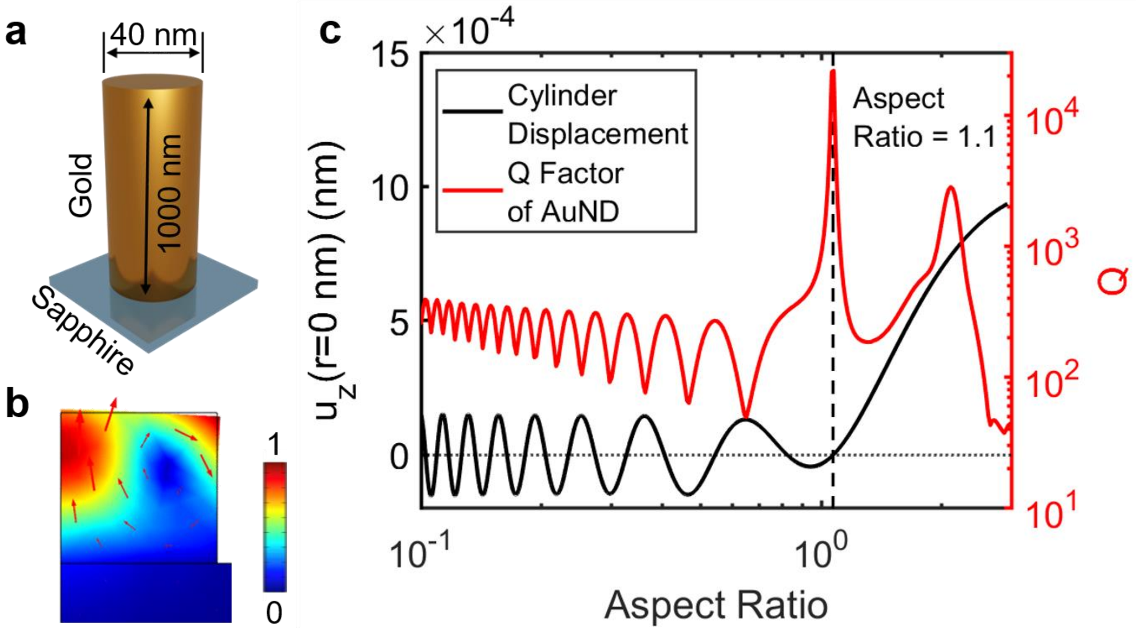

Figure 6: Using the model of a long cylinder, the Q-Factor enhancement in AuNDs depends on displacement nodes at the particle-substrate interface. a) Schematic for the model system of a long Au cylinder that was fixed onto a sapphire substrate. The diameter and height of the cylinder were set to 40 nm and 1000 nm, respectively. b) Representative displacement profile of an acoustic edge mode in an AuND with an aspect ratio of 2.1 on sapphire, color coated with the normalized displacement amplitude. The profile is a vertical cross-section of the right half of the AuND-substrate system. Only the edge mode was considered in the analysis and discussion of the cylinder. c) Comparison of the vertical displacement

u_z of the edge mode in the center of the cylinder on sapphire (black) and the simulated Q-Factors of the edge mode in AuNDs (red). The displacement in the cylinder was determined for each point along the cylinder height. Height positions were translated into aspect ratios for better comparison, using the cylinder diameter. The dashed vertical line indicates the overlap of a displacement node with the Q-Factor maximum at an aspect ratio of 1.1. The dotted horizontal indicates zero displacement for better visualization.

The model of a long cylinder confirmed enhancement of the Q-Factor as a function of displacement at the interface, leading to discrete maxima for certain aspect ratios. In this comparison, at each aspect ratio, the cylinder represented the limiting case of an AuND with an edge mode at its top, thus isolated from the substrate and only inducing small vertical displacements that caused loss of acoustic energy. However, the model revealed periodic nodes in these vertical displacements. By matching the aspect ratio of an AuND with the location of a displacement node in the cylinder, the displacements at the AuND-substrate interface can be eliminated and a minimum loss of acoustic energy can be achieved (see Figure S11 for further visualization). As shown in Figure 6c, this simple model predicted a displacement node at an aspect ratio of 1.1, thus confirming that the previously discussed first maximum in Q-Factor for AuNDs on sapphire is the result of minimized displacement at the AuND-substrate interface. For larger aspect ratios, the simple isolation of the edge mode from the substrate does not strictly apply any longer, leading to more complicated displacement profiles at the AuND-substrate interface, as, for example, shown for mode **V** at aspect ratio 4 in Figure 4. Thus, the displacements at the cylinder center alone are not sufficient to describe the acoustic Q-Factors, and the displacements across the entire particle-substrate contact area has to be considered to account for potential displacement minima.

Based on these results, we propose the following description of acoustic damping in lithographically prepared AuNDs. Both intrinsic and extrinsic damping must be considered, as shown by the discrepancy between experimental Q-Factors and simulated Q_{ext} factors. Intrinsic damping strongly damps the acoustic vibrations due to the polycrystallinity of the structures and can suppress enhanced Q-Factors even when reduced extrinsic damping is achieved. Previous studies have reported Q-Factors of ~10 for Au nanorings and weakly bound AuNDs,[28, 37] ~50 for Au nanorods,[38] and ~70 for strongly bound AuNDs and AuNDs on pillars.[39, 40] The wide range of Q-Factors, therefore, indicates that intrinsic damping can be reduced. We suggest that polycrystallinity can be minimized through control of the lithographic process, especially the use of slow evaporation rates for crystal growth and a high vacuum for minimized contamination. Extrinsic damping of substrate-supported AuNDs predominantly depends on the mechanical displacement at the particle-substrate interface and varies strongly between different acoustic modes. The acoustic modes of AuNDs change with the particle-substrate binding strength and become aspect ratio dependent, providing a tool to control extrinsic damping.

In the case of weak binding, the acoustic modes of AuNDs approximately correspond to those of a free disk. The weak particle-substrate coupling limits the loss of acoustic energy into the substrate because, due to its high excitation and detection efficiencies,[39] only the in-plane breathing mode is observed in the experiment. The in-plane breathing mode exhibits a mostly horizontal displacement direction and remains unchanged over a large aspect ratio range. The horizontal directionality of the AuND vibrations limits extrinsic damping, and the Q-Factors appear constant for varying aspect ratios and substrates. As a result, acoustic damping of weakly bound AuNDs is dominated by intrinsic effects. However, small effects of the substrate can be observed through increased acoustic frequencies compared to simulations of a completely free disk.

For strong binding, the substrate restricts the mechanical displacements within the particle and creates new acoustic modes. The displacement profiles of the new modes contain both horizontal and vertical components that change with the aspect ratio. Aspect ratio-dependent Q-Factors are generated as a result, with large Q-Factor enhancements occurring when displacement minima are located at the particle-substrate interface due to minimized loss of acoustic energy into the substrate. Lastly, the acoustic mode profiles of strongly bound AuNDs also depend on the relative acoustic impedances of particles and substrate. Smaller impedance mismatches create narrow Q-Factor maxima with respect to the aspect ratio, shift the maxima towards smaller aspect ratios, and increase the maximum achievable Q-Factor. Therefore, under the condition of strong binding, large acoustic Q-Factors in AuNDs can be engineered through the substrate material, aspect ratio, and binding strength. Based on comparable observations of Au nanocrosses,[34] we propose that this mechanism can be applied to arbitrary particle shapes. Although we do not consider hybridization of acoustic modes within the AuNDs and cannot exclude their importance, we find excellent agreement with recent theoretical investigations that have interpreted enhanced Q-Factors as a result of radiative coupling between particle modes displaying similar frequencies.[53]

The particle fabrication process is of utmost importance for the experimental realization of large Q-Factors with lithographically prepared nanostructures. While the particle crystallinity directly determines intrinsic damping, the quality of the particle-substrate interface is crucial to establish strong binding and control the extrinsic damping. Therefore, the potential to obtain large Q-Factors through both maximized Q_{int} and Q_{ext} relies on the fabrication and resulting particle quality. Indeed, our measurements of AuNDs on a sapphire substrate without Ti adhesion layers did not exhibit the enhanced acoustic Q-Factors that were predicted by simulations and reported by a previous study (Figure S12).[39] Instead, the experimental results agreed well with the in-plane breathing mode of a free disk (Figure S13). We, therefore, conclude that strong binding was not accomplished, most likely due to an imperfect sample fabrication, consistent with the sensitivity of direct metal-substrate interfaces to the fabrication process and elevating the use of adhesion layers as a robust and proven method to accomplish strong binding.[59] Furthermore, internal crystallinity and surface binding strength should be correlated, making it difficult if not impossible to lithographically fabricate high-quality nanostructures on a support while remaining in the regime of weak substrate coupling to isolate only the in-plane breathing mode of a free particle.

Conclusion

We studied the effect of strong particle-substrate binding on the acoustic Q-Factors of lithographically prepared AuNDs with Ti adhesion layers on glass substrates using single-particle transient transmission spectroscopy and FEM simulations. We found that strong binding modifies the acoustic properties of the AuNDs, creating several new hybridized modes whose displacement profiles are aspect ratio dependent. We identified that the displacements at the AuND-substrate interface were most important for the loss of acoustic energy through extrinsic damping, with small displacements at the interface diminishing the energy transfer into the substrate and thus giving the largest Q-Factors. Weakly bound AuNDs approximately exhibited the acoustic behavior of a free AuND, with a single acoustic mode observed corresponding to the horizontal in-plane breathing mode. Because the displacement profile of this mode did not change with aspect ratio, the extrinsic damping and thus the Q-Factor was found to be constant for all studied aspect ratios.

The aspect ratio dependent mode hybridization between the AuNDs and glass substrate for thick adhesion layers was found to cause distinct displacement minima at the AuND-substrate interface and hence Q-Factor enhancements for specific geometries. This effect was reproduced for sapphire as a substrate material through additional simulations. By switching to sapphire while maintaining strong binding, the acoustic impedance mismatch was decreased, leading to even larger Q-Factor maxima, but at smaller aspect ratios. Our results therefore rationalize the large spread of Q-Factors reported for lithographically prepared nanostructures and uncover the underlying mechanism of resonator geometry and impedance mismatch dependent mode hybridization that minimizes extrinsic damping. Under such optimized conditions, while carefully controlling metal evaporation to create strongly surface bound and high quality structures, it is then possible to generate hybridized acoustic modes with very large Q-Factors for lithographically fabricated resonators, despite intrinsic damping due to polycrystalline defects. Finally, the ability to controllably transform these nanoparticles from flawed towards efficient acoustic resonators with large Q-Factors through the control of substrate binding and impedance as well as resonator geometry opens the door to applications in sensing and acoustic signal generation.

Associated Content

Supporting Information

Schematic of the transient transmission microscope; plasmon resonances of AuNDs; spatial resolution with refractive objective; reproducibility of transient transmission measurement; additional details on FEM simulations and AuND geometry; SEM images of AuNDs; acoustic frequencies versus inverse AuND diameter; tabulated values of acoustic frequencies and Q-Factors for individual aspect ratios; acoustic Q-Factor versus aspect ratio; Q-Factor dependence on acoustic impedance; visualization of displacement in long cylinder.

Author Information

Corresponding Author

Stephan Link - Department of Chemistry, Department of Electrical and Computer Engineering, and Smalley-Curl Institute, NSF Center for Adapting Flaws into Features, Rice University, Houston, Texas 77005, United States; orcid.org/00000002-4781-930X; Email: slink@rice.edu

Authors

Niklas Gross - Department of Chemistry, NSF Center for Adapting Flaws into Features, Rice University, Houston, Texas 77005, United States; orcid.org/0000-0002-2425-1029; Email: ng27@rice.edu

Mahyar Madadi - Department of Materials Physics, Research School of Physics, ANU College of Science, Canberra, ACT 2600, Australia; orcid.org/0000-0002-6296-9082; Email: mahyar.madadi@gmail.com

Behnaz Ostovar - Department of Electrical and Computer Engineering, NSF Center for Adapting Flaws into Features, Rice University, Houston, Texas 77005, United States; orcid.org/00000001-6522-1806

Pratiksha D. Dongare - Department of Electrical and Computer Engineering, Rice University, Houston, Texas 77005, United States;.org/0000-0003-0224-8109

Lauren A. McCarthy - Department of Chemistry, Rice University, Houston, Texas 77005, United States; Present Address: Department of Chemistry, University of Michigan, Ann Arbor, Michigan, 48109 United States; org/0000-0002-9646-5333

Wei-Yi Chiang - Department of Chemistry, Rice University, Houston, Texas 77005, United States; Present Address: Department of Chemistry, National Kaohsiung Normal University, Kaohsiung City 82444, Taiwan; orcid.org/0000-0002-1131-0536

Wei-Shun Chang - Department of Chemistry, Rice University, Houston, Texas 77005, United States; Present Address: Department of Chemistry and Biochemistry, University of Massachusetts Dartmouth, North Dartmouth, Massachusetts 02747, United States; orcid.org/0000-0002-0251-4449

Naomi J. Halas - Department of Electrical and Computer Engineering, Department of Chemistry, Department of Physics and Astronomy, and Smalley Curl Institute, Rice University, Houston, Texas 77005, United States; orcid.org/0000-0002-8461-8494

Christy F. Landes − Department of Chemistry, Department of Electrical and Computer Engineering, Department of Chemical and Biomolecular Engineering, and Smalley-Curl Institute, NSF Center for Adapting Flaws into Features, Rice University, Houston, Texas 77005, United States; orcid.org/0000-0003-4163-6497

John E. Sader - Graduate Aerospace Laboratories, California Institute of Technology, Pasadena, California 91125, United States; orcid.org/0000-0002-7096-0627

Author Contributions

All authors have given approval for the final version of the manuscript.

Acknowledgements

This work was funded by the National Science Foundation, Center for Adapting Flaws into Features (NSF CHE-2124983). S.L. thanks the Robert A. Welch Foundation for support through the Charles W. Duncan, Jr.-Welch Chair in Chemistry (C-0002). C.F.L acknowledges funding from the Robert A. Welch Foundation (C-1787) and support through the Kenneth S. Pitzer-Schlumberger Chair in Chemistry. N.J.H. acknowledges funding from the Robert A. Welch Foundation (C-1220). L.A.M. acknowledges the National Science Foundation Research Fellowship Program (1842494) for support. This work was conducted in part using resources of the Shared Equipment Authority at Rice University.

Abbreviations

Au, gold; Ti, titanium; AuND, gold nanodisk; FEM, finite element method; SEM, scanning electron microscopy; IPA, isopropyl alcohol; PMMA, poly(methyl methacrylate); MIBK, methyl isobutyl ketone.

References

(1) Naik, A. K.; Hanay, M. S.; Hiebert, W. K.; Feng, X. L.; Roukes, M. L. Towards Single-Molecule Nanomechanical Mass Spectrometry. *Nat. Nanotechnol.* **2009**, *4*, 445-450.
(2) Ruijgrok, P. V.; Zijlstra, P.; Tchebotareva, A. L.; Orrit, M. Damping of Acoustic Vibrations of Single Gold Nanoparticles Optically Trapped in Water. *Nano Lett.* **2012**, *12*, 1063-1069.
(3) Fernandes, B. D.; Vilar-Vidal, N.; Baida, H.; Masse, P.; Oberle, J.; Ravaine, S.; Treguer-Delapierre, M.; Saviot, L.; Langot, P.; Burgin, J. Acoustic Vibrations of Core-Shell Nanospheres: Probing the Mechanical Contact at the Metal-Dielectric Interface. *J. Phys. Chem. C* **2018**, *122*, 9127-9133.
(4) Maioli, P.; Stoll, T.; Sauceda, H. E.; Valencia, I.; Demessence, A.; Bertorelle, F.; Crut, A.; Vallee, F.; Garzon, I. L.; Cerullo, G.; et al. Mechanical Vibrations of Atomically Defined Metal Clusters: From Nano- to Molecular-Size Oscillators. *Nano Lett.* **2018**, *18*, 6842-6849.
(5) Stoll, T.; Maioli, P.; Crut, A.; Burgin, J.; Langot, P.; Pellarin, M.; Sanchez-Iglesias, A.; Rodriguez-Gonzalez, B.; Liz-Marzan, L. M.; Del Fatti, N.; et al. Ultrafast Acoustic Vibrations of Bimetallic Nanoparticles. *J. Phys. Chem. C* **2015**, *119*, 1591-1599.
(6) Medeghini, F.; Rouxel, R.; Crut, A.; Maioli, P.; Rossella, F.; Banfi, F.; Vallee, F.; Del Fatti, N. Signatures of Small Morphological Anisotropies in the Plasmonic and Vibrational Responses of Individual Nano-Objects. *J. Phys. Chem. Lett.* **2019**, *10*, 5372-5380.
(7) Wang, L.; Nishijima, Y.; Ueno, K.; Misawa, H.; Tamai, N. Effect of Dipole Coupling on near-Ir Lspr and Coherent Phonon Vibration of Periodic Gold Pair Nanocuboids. *J. Phys. Chem. C* **2012**, *116*, 17838-17846.
(8) Dowgiallo, A. M.; Schwartzberg, A. M.; Knappenberger, K. L. Structure-Dependent Coherent Acoustic Vibrations of Hollow Gold Nanospheres. *Nano Lett.* **2011**, *11*, 3258-3262.
(9) Ahmed, A.; Pelton, M.; Guest, J. R. Understanding How Acoustic Vibrations Modulate the Optical Response of Plasmonic Metal Nanoparticles. *ACS Nano* **2017**, *11*, 9360-9369.
(10) Hartland, G. V. Optical Studies of Dynamics in Noble Metal Nanostructures. *Chem. Rev.* **2011**, *111*, 3858-3887.
(11) Beane, G.; Devkota, T.; Brown, B. S.; Hartland, G. V. Ultrafast Measurements of the Dynamics of Single Nanostructures: A Review. *Rep. Prog. Phys.* **2018**, *82*, 016401.
(12) Liu, T. R.; Pagliano, F.; van Veldhoven, R.; Pogoretskiy, V.; Jiao, Y. Q.; Fiore, A. Integrated Nano-Optomechanical Displacement Sensor with Ultrawide Optical Bandwidth. *Nat. Commun.* **2020**, *11*, 2407.
(13) Sansa, M.; Defoort, M.; Brenac, A.; Hermouet, M.; Banniard, L.; Fafin, A.; Gely, M.; Masselon, C.; Favero, I.; Jourdan, G.; et al. Optomechanical Mass Spectrometry. *Nat. Commun.* **2020**, *11*, 3781
(14) Lu, H.; Wang, C. Q.; Yang, L.; Jing, H. Optomechanically Induced Transparency at Exceptional Points. *Phys. Rev. Appl.* **2018**, *10*, 014006.
(15) Gusev, V. E.; Ruello, P. Advances in Applications of Time-Domain Brillouin Scattering for Nanoscale Imaging. *Appl. Phys. Rev.* **2018**, *5*, 031101.
(16) Tamayo, J.; Kosaka, P. M.; Ruz, J. J.; San Paulo, A.; Calleja, M. Biosensors Based on Nanomechanical Systems. *Chem. Soc. Rev.* **2013**, *42*, 1287-1311.
(17) Kosaka, P. M.; Pini, V.; Ruz, J. J.; da Silva, R. A.; Gonzalez, M. U.; Ramos, D.; Calleja, M.; Tamayo, J. Detection of Cancer Biomarkers in Serum Using a Hybrid Mechanical and Optoplasmonic Nanosensor. *Nat. Nanotechnol.* **2014**, *9*, 1047-1053.
(18) Hanay, M. S.; Kelber, S.; Naik, A. K.; Chi, D.; Hentz, S.; Bullard, E. C.; Colinet, E.; Duraffourg, L.; Roukes, M. L. Single-Protein Nanomechanical Mass Spectrometry in Real Time. *Nat. Nanotechnol.* **2012**, *7*, 602-608.
(19) Devkota, T.; Yu, K.; Hartland, G. V. Mass Loading Effects in the Acoustic Vibrations of Gold Nanoplates. *Nanoscale* **2019**, *11*, 16208-16213.
(20) Fernandes, B. D.; Spuch-Calvar, M.; Baida, H.; Treguer-Delapierre, M.; Oberle, J.; Langot, P.; Burgin, J. Acoustic Vibrations of Au Nano-Bipyramids and Their Modification under Ag Deposition: A Perspective for the Development of Nanobalances. *ACS Nano* **2013**, *7*, 7630-7639.

(21) Girard, A.; Saviot, L.; Pedetti, S.; Tessier, M. D.; Margueritat, J.; Gehan, H.; Mahler, B.; Dubertret, B.; Mermet, A. The Mass Load Effect on the Resonant Acoustic Frequencies of Colloidal Semiconductor Nanoplatelets. *Nanoscale* **2016**, *8*, 13251-13256.
(22) Yu, K.; Sader, J. E.; Zijlstra, P.; Hong, M.; Xu, Q.-H.; Orrit, M. Probing Silver Deposition on Single Gold Nanorods by Their Acoustic Vibrations. *Nano Lett.* **2014**, *14*, 915-922.
(23) Safavi-Naeini, A. H.; Van Thourhout, D.; Baets, R.; Van Laer, R. Controlling Phonons and Photons at the Wavelength Scale: Integrated Photonics Meets Integrated Phononics. *Optica* **2019**, *6*, 410-410.
(24) Wenzler, J. S.; Dunn, T.; Toffoli, T.; Mohanty, P. A Nanomechanical Fredkin Gate. *Nano Lett.* **2014**, *14*, 89-93.
(25) Chappanda, K. N.; Ilyas, S.; Kazmi, S. N. R.; Holguin-Lerma, J.; Batra, N. M.; Costa, P. M. F. J.; Younis, M. I. A Single Nano Cantilever as a Reprogrammable Universal Logic Gate. *J. Micromech. Microeng.* **2017**, *27*, 045007.
(26) Ostovar, B.; Su, M.-N.; Renard, D.; Clark, B. D.; Dongare, P. D.; Dutta, C.; Gross, N.; Sader, J. E.; Landes, C. F.; Chang, W.-S.; et al. Acoustic Vibrations of Al Nanocrystals: Size, Shape, and Crystallinity Revealed by Single-Particle Transient Extinction Spectroscopy. *J. Phys. Chem. A* **2020**, *124*, 3924-3934.
(27) Yu, K.; Zijlstra, P.; Sader, J. E.; Xu, Q. H.; Orrit, M. Damping of Acoustic Vibrations of Immobilized Single Gold Nanorods in Different Environments. *Nano Lett.* **2013**, *13*, 2710-2716.
(28) Yi, C. Y.; Su, M. N.; Dongare, P. D.; Chakraborty, D.; Cai, Y. Y.; Marolf, D. M.; Kress, R. N.; Ostovar, B.; Tauzin, L. J.; Wen, F. F.; et al. Polycrystallinity of Lithographically Fabricated Plasmonic Nanostructures Dominates Their Acoustic Vibrational Damping. *Nano Lett.* **2018**, *18*, 3494-3501.
(29) Wang, J. Z.; Yang, Y.; Wang, N.; Yu, K.; Hartland, G. V.; Wang, G. P. Long Lifetime and Coupling of Acoustic Vibrations of Gold Nanoplates on Unsupported Thin Films. *J. Phys. Chem. A* **2019**, *123*, 10339-10346.
(30) Major, T. A.; Crut, A.; Gao, B.; Lo, S. S.; Del Fatti, N.; Vallee, F.; Hartland, G. V. Damping of the Acoustic Vibrations of a Suspended Gold Nanowire in Air and Water Environments. *Phys. Chem. Chem. Phys.* **2013**, *15*, 4169-4176.
(31) Yu, K.; Major, T. A.; Chakraborty, D.; Devadas, M. S.; Sader, J. E.; Hartland, G. V. Compressible Viscoelastic Liquid Effects Generated by the Breathing Modes of Isolated Metal Nanowires. *Nano Lett.* **2015**, *15*, 3964-3970.
(32) Wang, J. Z.; Yu, K.; Yang, Y.; Hartland, G. V.; Sader, J. E.; Wang, G. P. Strong Vibrational Coupling in Room Temperature Plasmonic Resonators. *Nat. Commun.* **2019**, *10*.
(33) Yi, C. Y.; Dongare, P. D.; Su, M. N.; Wang, W. X.; Chakraborty, D.; Wen, F. F.; Chang, W. S.; Sader, J. E.; Nordlander, P.; Halas, N. J.; et al. Vibrational Coupling in Plasmonic Molecules. *P. Natl. Acad. Sci. U. S. A.* **2017**, *114*, 11621-11626.
(34) O'Brien, K.; Lanzillotti-Kimura, N. D.; Rho, J.; Suchowski, H.; Yin, X. B.; Zhang, X. Ultrafast Acousto-Plasmonic Control and Sensing in Complex Nanostructures. *Nat. Commun.* **2014**, *5*, 4042
(35) Della Picca, F.; Berte, R.; Rahmani, M.; Albella, P.; Bujjamer, J. M.; Poblet, M.; Cortes, E.; Maier, S. A.; Bragas, A. V. Tailored Hypersound Generation in Single Plasmonic Nanoantennas. *Nano Lett.* **2016**, *16*, 1428-1434.
(36) Chang, W. S.; Wen, F. F.; Chakraborty, D.; Su, M. N.; Zhang, Y.; Shuang, B.; Nordlander, P.; Sader, J. E.; Halas, N. J.; Link, S. Tuning the Acoustic Frequency of a Gold Nanodisk through Its Adhesion Layer. *Nat. Commun.* **2015**, *6*, 7022.
(37) Kelf, T. A.; Tanaka, Y.; Matsuda, O.; Larsson, E. M.; Sutherland, D. S.; Wright, O. B. Ultrafast Vibrations of Gold Nanorings. *Nano Lett.* **2011**, *11*, 3893-3898.
(38) Boggiano, H. D.; Berte, R.; Scarpettini, A. F.; Cortes, E.; Maier, S. A.; Bragas, A. V. Determination of Nanoscale Mechanical Properties of Polymers Via Plasmonic Nanoantennas. *ACS Photonics* **2020**, *7*, 1403-1409.
(39) Medeghini, F.; Crut, A.; Gandolfi, M.; Rossella, F.; Maioli, P.; Vallee, F.; Banfi, F.; Del Fatti, N. Controlling the Quality Factor of a Single Acoustic Nanoresonator by Tuning Its Morphology. *Nano Lett.* **2018**, *18*, 5159-5166.

(40) Delalande, R.; Bonhomme, J.; Dandeu, E.; Becerra, L.; Belliard, L. Substrate Influence on the Vibrational Response of Gold Nanoresonators: Towards Tunable Acoustic Nanosources. *Phys. Rev. B* **2022**, *105*, 035422
(41) Chakraborty, D.; van Leeuwen, E.; Pelton, M.; Sader, J. E. Vibration of Nanoparticles in Viscous Fluids. *J. Phys. Chem. C* **2013**, *117*, 8536-8544.
(42) Pelton, M.; Chakraborty, D.; Malachosky, E.; Guyot-Sionnest, P.; Sader, J. E. Viscoelastic Flows in Simple Liquids Generated by Vibrating Nanostructures. *Phys. Rev. Lett.* **2013**, *111*, 244502
(43) Chakraborty, D.; Hartland, G. V.; Pelton, M.; Sader, J. E. When Can the Elastic Properties of Simple Liquids Be Probed Using High-Frequency Nanoparticle Vibrations? *J. Phys. Chem. C* **2018**, *122*, 13347-13353.
(44) Pelton, M.; Sader, J. E.; Burgin, J.; Liu, M. Z.; Guyot-Sionnest, P.; Gosztola, D. Damping of Acoustic Vibrations in Gold Nanoparticles. *Nat. Nanotechnol.* **2009**, *4*, 492-495.
(45) Marty, R.; Arbouet, A.; Girard, C.; Mlayah, A.; Paillard, V.; Lin, V. K.; Teo, S. L.; Tripathy, S. Damping of the Acoustic Vibrations of Individual Gold Nanoparticles. *Nano Lett.* **2011**, *11*, 3301-3306.
(46) Pelton, M.; Wang, Y. L.; Gosztola, D.; Sader, J. E. Mechanical Damping of Longitudinal Acoustic Oscillations of Metal Nanoparticles in Solution. *J. Phys. Chem. C* **2011**, *115*, 23732-23740.
(47) Cardinal, M. F.; Mongin, D.; Crut, A.; Maioli, P.; Rodriguez-Gonzalez, B.; Perez-Juste, J.; Liz-Marzan, L. M.; Del Fatti, N.; Vallee, F. Acoustic Vibrations in Bimetallic Au@Pd Core-Shell Nanorods. *J. Phys. Chem. Lett.* **2012**, *3*, 613-619.
(48) Burgin, J.; Langot, P.; Del Fatti, N.; Vallee, F.; Huang, W.; El-Sayed, M. A. Time-Resolved Investigation of the Acoustic Vibration of a Single Gold Nanoprism Pair. *J. Phys. Chem. C* **2008**, *112*, 11231-11235.
(49) Wang, J. Z.; Li, M. Y.; Jiang, Y. Q.; Yu, K.; Hartland, G. V.; Wang, G. P. Polymer Dependent Acoustic Mode Coupling and Hooke's Law Spring Constants in Stacked Gold Nanoplates. *J. Chem. Phys.* **2021**, *155*, 144701
(50) Yu, K.; Yang, Y.; Wang, J. Z.; Hartland, G. V.; Wang, G. P. Nanoparticle-Fluid Interactions at Ultrahigh Acoustic Vibration Frequencies Studied by Femtosecond Time-Resolved Microscopy. *ACS Nano* **2021**, *15*, 1833-1840.
(51) Gan, Y.; Sun, Z. Crystal Structure Dependence of the Breathing Vibration of Individual Gold Nanodisks Induced by the Ultrafast Laser. *Appl. Opt.* **2019**, *58*, 213-218.
(52) Hartland, G. V.; Hu, M.; Sader, J. E. Softening of the Symmetric Breathing Mode in Gold Particles by Laser-Induced Heating. *J. Phys. Chem. B* **2003**, *107*, 7472-7478.
(53) Crut, A. Substrate-Supported Nano-Objects with High Vibrational Quality Factors. *J. Appl. Phys.* **2022**, *131*, 244301
(54) Hu, M.; Wang, X.; Hartland, G. V.; Mulvaney, P.; Juste, J. P.; Sader, J. E. Vibrational Response of Nanorods to Ultrafast Laser Induced Heating: Theoretical and Experimental Analysis. *J. Am. Chem. Soc.* **2003**, *125*, 14925-14933.
(55) Giovannini, T.; Nicoli, L.; Lafiosca, P.; Nicoli, L.; Castagnola, M.; Illobre, P. G.; Corni, S.; Cappelli, C. Do We Really Need Quantum Mechanics to Describe Plasmonic Properties of Metal Nanostructures? *ACS Photonics* **2022**, *9*, 3025-3034.
(56) Lafiosca, P.; Giovannini, T.; Benzi, M.; Cappelli, C. Going Beyond the Limits of Classical Atomistic Modeling of Plasmonic Nanostructures. *J. Phys. Chem. C* **2021**, *125*, 23848-23863.
(57) Sader, J. E.; Hartland, G. V.; Mulvaney, P. Theory of Acoustic Breathing Modes of Core-Shell Nanoparticles. *J. Phys. Chem. B* **2002**, *106*, 1399-1402.
(58) Mongin, D.; Juve, V.; Maioli, P.; Crut, A.; Del Fatti, N.; Vallee, F.; Sanchez-Iglesias, A.; Pastoriza-Santos, I.; Liz-Marzan, L. M. Acoustic Vibrations of Metal-Dielectric Core-Shell Nanoparticles. *Nano Lett.* **2011**, *11*, 3016-3021.
(59) Nagata, H.; Shinriki, T.; Shima, K.; Tamai, M.; Haga, E. M. Improvement of Bonding Strength between Au Ti and Sio2 Films by Si Layer Insertion. *J. Vac. Sci. Technol., A* **1999**, *17*, 1018-1023.